Rationally designed fluorogenic protease reporter visualizes spatiotemporal dynamics of apoptosis in vivo

Tsz-Leung To[a,b], Beverly J. Piggott[b,c,d], Kalpana Makhijani[a,b], Dan Yu[a,b], Yuh Nung Jan[b,c,d,1], and Xiaokun Shu[a,b,1]

Departments of [a]Pharmaceutical Chemistry and [c]Physiology, [b]Cardiovascular Research Institute, and [d]Howard Hughes Medical Institute, University of California, San Francisco, CA 94158

Fluorescence resonance energy transfer-based reporters have been widely used in imaging cell signaling; however, their in vivo application has been handicapped because of poor signal. Although fluorogenic reporters overcome this problem, no such reporter of proteases has been demonstrated for in vivo imaging. Now we have redesigned an infrared fluorescent protein so that its chromophore incorporation is regulated by protease activity. Upon protease activation, the infrared fluorogenic protease reporter becomes fluorescent with no requirement of exogenous cofactor. To demonstrate biological applications, we have designed an infrared fluorogenic executioner-caspase reporter, which reveals spatiotemporal coordination between cell apoptosis and embryonic morphogenesis, as well as dynamics of apoptosis during tumorigenesis in Drosophila. The designed scaffold may be used to engineer reporters of other proteases with specific cleavage sequence.

protease | fluorogenic reporters | bacterial phytochrome | apoptosis | tumor development

Proteases play fundamental roles in almost every major biological process. The human genome contains ~600 proteases and homologs, similar to the number of protein kinases (~500) (1). Changes to proteolytic systems lead to many diseases, including cancer (2). To visualize spatiotemporal dynamics of protease activity in vivo, genetically encoded fluorogenic reporters would be ideal because of their strong signal, which overcomes tissue autofluorescence and cell heterogeneity. Such reporters would thus be valuable in understanding the role of proteases in animal development and disease. However, no fluorogenic reporter of proteases based on a genetically encoded fluorescent probe, such as GFP, has been demonstrated for in vivo imaging. This might suggest an intrinsic limitation of the protein topology of GFP, which was introduced into molecular imaging two decades ago. Recently engineered infrared fluorescent proteins (IFPs) from bacterial phytochromes (BphPs) provide a new scaffold for designing such reporters (3, 4).

BphPs belong to the phytochrome (Phy) red/far-red photoreceptor superfamily (5). IFPs are composed of the N-terminal PAS and GAF domains of BphPs, and autocatalytically incorporate the chromophore biliverdin (BV) (Fig. 1A). BV is a catabolic metabolite of heme by heme oxygenase and is nonfluorescent by itself. BV binds to the GAF domain noncovalently and forms a thioether bond with a conserved cysteine near N terminus of IFPs (3, 6).

Results and Discussion

Rational Design of an Infrared Fluorogenic Protease Reporter.
To design an infrared fluorogenic protease reporter that becomes fluorescent upon protease activation, we have re-engineered IFP so that its chromophore incorporation is regulated by protease activity. To engineer such regulation into IFP, we harnessed potential physical and chemical mechanisms of BV binding to IFPs: the catalytic cysteine is physically close to the BV-binding cavity in the GAF domain, which presumably facilitates formation of the thioether bond (Fig. 1A). Thus, it appears that physical

proximity of the cysteine to the binding cavity is essential for the chromophore incorporation (Movie S1). We then hypothesized that if the cysteine is physically displaced, the incorporation of BV may be abolished.

To displace the cysteine from the binding cavity, we redesigned IFP (Fig. 1B). First, we circularly permutated the protein so that the native N and C termini are linked by a protease cleavage sequence, with a new opening between the PAS and GAF domains. Then we added split GFP (7) to the circularly permutated IFP. This approach ensures that after protease cleavage, the redesigned IFP will remain intact. Finally, we truncated the native N and C termini so that the distance between the cysteine and the carboxyl end of GAF is larger than the length of the protease cleavage sequence (Movies S2 and S3). This approach results in the cysteine being displaced from the binding cavity, and no incorporation of the chromophore. In this inactive state, the designed infrared fluorogenic protease reporter (iProtease) is not infrared fluorescent. Once the cleavage sequence is recognized and cleaved by the cognate protease, the cysteine is free to return to the binding cavity. BV can then form a bond with the cysteine and be incorporated into the protein. Therefore, once activated by its protease, the active iProtease becomes infrared fluorescent. On the other hand, both inactive and active iProtease are green fluorescent from the recombined split GFP, independent of protease's
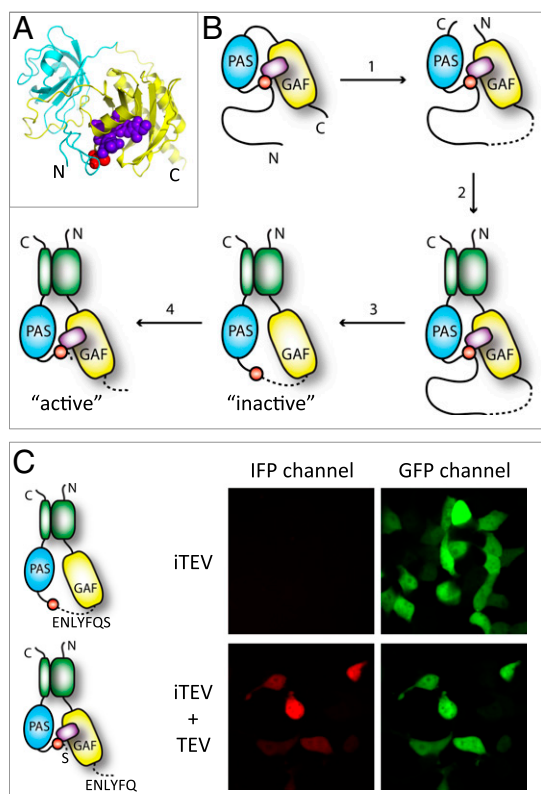
Fig. 1. Rational design of genetically encoded iProtease. (*A*) Modeled structure of an IFP. The PAS and GAF domains are shown in cyan and yellow, respectively. The catalytic cysteine and the chromophore (BV) are shown in red and purple, respectively. (*B*) Design strategy. IFP is shown by cartoon (BV in purple, cysteine in orange). The dashed line represents protease cleavage sequence. The large and small green boxes represent amino (N) and carboxyl (C) part of split GFP. Steps of the design: step 1, circular permutation; step 2, adding N- and C-part of the split GFP; step 3, truncation at the old N and C terminus of IFP; step 4, protease cleavage (activation). (*C*) Proof of principle. Fluorescence images of HEK293 expressing: iTEV (*Upper*); iTEV and TEV protease (*Lower*). (Magnification: *C*, 40×.)

activity, which can be used to monitor the reporter's expression and to mark all of the cells in the tissue of interest.

As a proof of concept, we designed an infrared fluorescent tobacco etch virus (TEV) protease sensor (iTEV) by designing the TEV cleavage sequence into the iProtease scaffold. Human embryonic kidney 293 (HEK293) cells expressing iTEV were green but not infrared fluorescent (Fig. 1*C*), consistent with an inactive iTEV. Coexpression of the TEV protease resulted in both green and infrared fluorescence, consistent with an active iTEV (Fig. 1*C*). Both green and infrared fluorescence require no exogenous cofactor.

Characterization of the Protease Reporter. To confirm the mechanism of iProtease, we first measured the spectra of purified iTEV. The active iTEV has two main absorbance peaks at 480 and 680 nm (Fig. 2 *A* and *B*), which are characteristic of split-GFP's (7) and IFP's absorbance (4). In contrast, the inactive iTEV does not contain the long-wavelength band (Fig. 2*B*), indicating that it does not incorporate BV. Excitation of the short- and long-wavelength bands resulted in green and infrared fluorescence (Fig. 2*C*), which correspond to GFP and IFP's fluorescence spectra.

We then measured the binding kinetics of BV to the activated sensor. We added BV to the cleaved iTEV purified from *Escherichia coli* in the absence of BV, and monitored the infrared fluorescence

as a function of time (Fig. 2*D*). The infrared fluorescence rises within 10 s, suggesting that BV binding to the activated sensor is rapid.

To determine whether the chromophore incorporation is covalent, we did gel electrophoresis of the active iTEV purified from *Escherichia coli* in a mixture of iTEV, TEV, and BV. The N-half of the sensor is expected to be 46 kDa and the C-half 15 kDa. Two bands revealed by Coomassie blue staining correspond to N- and C-half of the sensor with the expected molecular weight (Fig. 2*E*). We then did zinc-induced fluorescence assay (Fig. 2*E*, *Bottom*), which is a standard assay in characterizing covalent incorporation of bilin into phytochromes, based on the phenomena that bilin–zinc ion complex is orange fluorescent upon UV illumination (8, 9). We observed that zinc-induced orange fluorescence was at the same position as the C-half protein band visualized by Coomassie blue staining, demonstrating that BV is covalently incorporated because the proteins were denatured in the assay. As a control, we did not observe such orange fluorescence in the absence of BV (Fig. 2*E*).

We also characterized dependence of iProtease on the length of cleavage sequence (Fig. 2*A*). According to our design, if we increase the length to be close or longer than the distance between the cysteine and the carboxyl end of the GAF domain, the inactive sensor will eventually become fluorescent. To test this theory, we generated six iTEV derivatives, and together with iTEV the length spans from 9 (7 aa of the TEV consensus sequence plus 2 additional amino acids resulted from a cloning site) to 15 aa. The inactive derivatives remained nonfluorescent in the IFP channel up to 11 aa (Fig. 2 *F* and *G*). The derivatives became infrared fluorescent at 12 aa and the fluorescence increased and saturated at 14 aa. When the TEV was coexpressed, all of the derivatives were infrared fluorescent. These results support the "pulling" mechanism designed into iProtease.

Finally, we examined the protease specificity of our design. We created a Hepatitis C virus (HCV) NS3/4A protease sensor (iHCV). Our data indicated that iTEV was only activated by the TEV protease, whereas iHCV was only activated by the HCV protease (Fig. 2*H*). These results demonstrate that the iProtease scaffold can be highly specific.

Infrared Fluorescent Executioner-Caspase Reporter Visualizes Cell Apoptosis. To demonstrate biological applications of the iProtease technology, we created an infrared fluorescent executioner-caspase reporter (iCasper) (Fig. 3 *A* and *B*). Human glioblastoma LN229 cells expressing iCasper were green but not infrared fluorescent. Upon addition of staurosporine, which is a protein kinase inhibitor and induces apoptosis by activating caspase 3 (10), iCasper became infrared fluorescent as the cells underwent apoptosis (Fig. 3*C* and Movie S4). The onset of apoptosis in single cells varies between 1 and 6 h after addition of staurosporine (Fig. 3*D*), consistent with previous results (11). Activation of executioner caspases was confirmed by antibody staining (Fig. S1).

To demonstrate in vivo applications, we created a transgenic UAS-iCasper *Drosophila*. Because of the genetic tractability and plethora of available genetic tools, *Drosophila melanogaster* is an attractive model organism for investigation into animal development and disease. To demonstrate iCasper, we decided to visualize neuronal apoptosis in the developing CNS, where a subset of neurons have been shown to undergo apoptosis (12, 13). To visualize neuronal apoptosis, we expressed iCasper in the neurons using pan-neuronal *elav*-GAL4 driver. To distinguish individual cells, we crossed this line with a transgenic line expressing CD8-GFP in neurons that marks cell membrane. iCasper visualized apoptotic neurons in the ventral nerve cord (VNC) as expected (Fig. S2*A*). Coexpression of the caspase inhibitor p35 abolished the infrared fluorescence in the VNC (Fig. S2*B*) (14), which confirms that iCasper reports caspase activity.

To demonstrate the utility of iCasper to capture apoptosis during animal development, we first conducted time-lapse
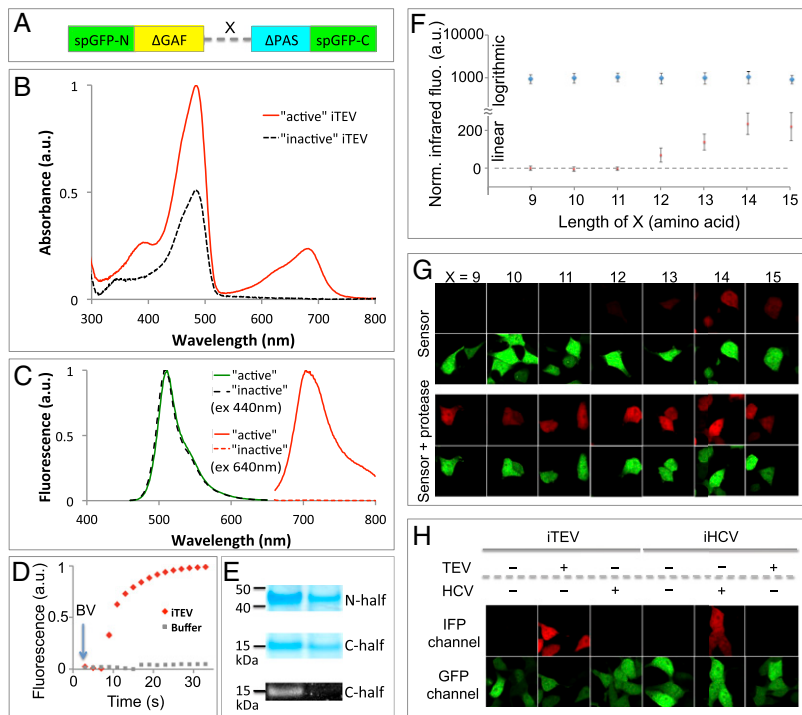
BIOCHEMISTRY

Fig. 2. Characterization of iProtease. (A) Schematic diagram. The dashed line represents the cleavage sequence with length x. (B) Absorbance spectra of the active and inactive iTEV. Note: active iTEV was prepared by purifying iTEV from the mixture of iTEV, TEV, and BV; inactive iTEV was prepared by purifying iTEV from the mixture of iTEV and BV. The inactive iTEV is normalized to 0.5 so that its spectrum does not overlap with that of active iTEV. (C) Emission spectra of active and inactive iTEV upon excitation at 440 or 640 nm. (D) Chromophore binding kinetics. (E) Coomassie blue staining and zinc-induced fluorescence assay (Bottom) of the active (Top) and activated (Middle) iTEV. (F) Normalized (by GFP) infrared fluorescence of iTEV (x = 9 aa) and its derivatives (x = 10–15) plotted against the length x. The red and blue squares correspond to cells expressing the sensor and the sensor plus protease, respectively. (G) Representative images of HEK293 cells expressing the iTEV and derivatives. (H) Specificity of iProtease: HEK293 cells expressing the iTEV or the HCV NS3/4A protease reporter (iHCV), with or without coexpression of the TEV or the NS3/4A protease. (Magnification: G and H, 40×.)

imaging of a small region of the VNC in intact *Drosophila* embryos, which revealed that infrared fluorescence appeared as the neurons began to round up and remained throughout cell blebbing and subsequent formation of apoptotic cell bodies (Fig. 4A and Movies S5 and S6), suggesting that iCasper reports real-time activation of the executioner caspases. This result is consistent with the rapid BV binding kinetics. It has previously been well characterized that during apoptosis cells first shrink, then round up because of cytoskeleton rearrangement, followed by membrane blebbing as a result of dynamic actin reorganization and contraction (15–17). Finally, the cells dismantle into apoptotic cell bodies that contain intact plasma membrane. iCasper visualizes apoptotic cells undergoing these structural changes along the entire time course of apoptosis. Therefore, iCasper is a robust caspase reporter that visualizes apoptosis in vivo.

To reveal spatiotemporal pattern of apoptosis in the CNS during development, we imaged the whole embryo at lower magnification. It indicated that apoptosis first occurred at posterior part of the VNC when this region moved toward anterior part (Movie S7). The number of apoptotic cells increased

significantly in the posterior part through the time course of VNC shortening. At later stage, apoptosis also occurred in the anterior part of VNC. Time-lapse imaging of the whole embryo also revealed that a significant portion of neurons in the brain underwent apoptosis at the late stage of embryo development when the brain moved deeper inside the embryo along the anterior-posterior direction (Movie S8). Although the purpose and molecular mechanisms of neuronal apoptosis in the *Drosophila* brain at this time are unclear, it is known in general that during development of neuronal circuits in the brain, neurons that fail to establish connections with other neurons are eliminated through apoptosis (18). It is believed that neurotrophins, which are important for neuronal survival, may be involved in this process. iCasper will be a useful tool to study function and to reveal molecular mechanisms of neuronal apoptosis in the developing brain.

iCasper Visualizes Spatiotemporal Dynamics of Apoptosis During Embryonic Morphogenesis. It has been well established that inhibition of apoptosis impairs morphogenesis of *Drosophila*
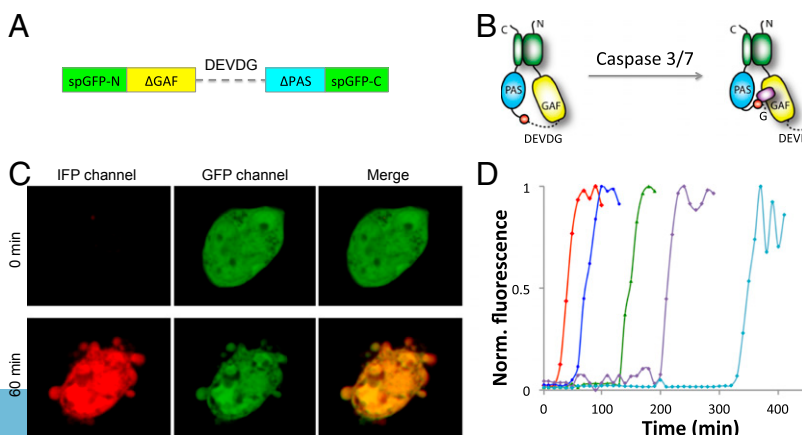

Fig. 3. Genetically encoded iCasper. (A) Construct of iCasper. (B) Cartoon showing working mechanism of iCasper before (Left) and after (Right) its cleavage and activation by executioner caspases. (C) Confocal images of human glioblastoma cells LN229 stably expressing iCasper before and after treatment with 1 μM staurosporin. See also Movie S4. (Magnification: 40×.) (D) Normalized infrared fluorescence of LN229 cells stably expressing iCasper reveals cell-to-cell heterogeneity of caspase activation upon addition of staurosporin. The infrared fluorescence was normalized by the green fluorescence based on confocal images of live cells after treatment with 1 μM staurosporin, which were collected every 10 min.
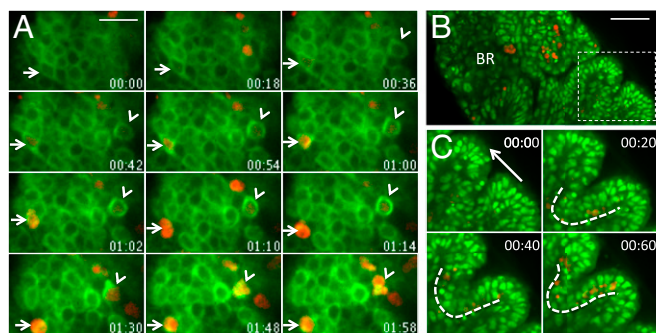
To et al.

Fig. 4. iCasper visualizes apoptosis and reveals correlation of apoptosis and morphogenesis in *Drosophila*. (*A*) Time-lapse images of neurons in the VNC in vivo reveal caspase activation and apoptotic cell shape change during CNS development. Two neurons undergoing apoptosis are pointed by the arrow and arrowhead. The number at the lower right corner of each panel refers to time (h:min). See also Movie S5. (Scale bar, 10 μm.) (*B*) *Drosophila* embryo around head region during morphogenesis. BR, brain. (Scale bar, 30 μm.) (*C*) Time-lapse images of *Drosophila* embryo around head region (outlined by the dashed box in *B*). The arrow points to the direction of morphogenetic movement. The dashed lines outline the distribution of apoptotic cells (in red). See also Movie S10. (Magnification: *C*, 40×.)

embryos, suggesting that apoptosis plays an essential role in embryo development (19, 20). However, it has remained unclear whether apoptosis is spatiotemporally correlated to morphogenesis. Imaging the embryo near stage 13 revealed that apoptosis mainly occurred around the head region with a characteristic spatial pattern (Fig. S3 and Movie S9). Time-lapse imaging of the head region from stages 12–16 revealed that apoptosis occurred around the same time as the segments dramatically changed shape before head involution. Moreover, the apoptotic cells were distributed near the edge of the moving segments (Fig. 4 *B* and *C* and Movie S10), suggesting that apoptosis is spatiotemporally correlated to morphogenesis. Furthermore, the apoptotic cell bodies were quickly taken up by large and motile cells, which appeared to move along the space between tissues and are presumably macrophages (Movie S10). Interestingly, the infrared fluorescence of iCasper remains inside these cells, demonstrating that iCasper is a robust reporter with the capacity to visualize apoptotic cell bodies even when they are phagocytosed.

iCasper Reveals Dynamics of Apoptosis During Tumorigenesis. To demonstrate application of iCasper in disease, we examined spatiotemporal dynamics of apoptosis during tumorigenesis because evasion of apoptosis is one of the hallmarks of cancer (21). We made use of a previously characterized brain tumor model generated by overexpressing the transcription factor Deadpan (Dpn) in the *Drosophila* larval brain (Fig. 5*A* and Fig. S4) (22–24). Throughout neural development, the stem cells of *Drosophia,* known as neuroblasts (NBs), proliferate to generate the nervous system of both larval and adult stages via asymmetric division, whereby NBs self-renew and generate daughter cells (Fig. 5*B*) (25, 26). Defects in the mechanisms controlling this process can lead to premature differentiation and an incomplete nervous system, or alternatively an excess of NBs that can lead to tumor formation (Fig. 5*C*) (25). Dpn is normally expressed in the NBs and intermediate neural progenitors (INPs) of the developing *Drosophila* brain and has roles in maintaining NB self-renewal and specification of the type II NB identity in larval brains (22–24). We ectopically overexpressed Dpn (*dpn^{OE}*) using the *insc*-GAL4 (GAL4^{1407} inserted in inscuteable promoter) driving expression in NBs, INPs, and GMCs (ganglion mother cells), which has been shown to lead to excessive NB proliferation at the expense of more differentiated cells, representing a tumor-

like state (22–24). The *dpn^{OE}* brain exhibited notable growth from 60 to 96 h after larval hatching (ALH) (Fig. S4). At 72 h ALH, the *dpn^{OE}* brain (*insc*-GAL4; UAS-*dpn*) is significantly larger than wild-type (Fig. 5 *D* and *E*, and Fig. S4 *C* and *D*), consistent with previous Dpn overexpression studies (22–24, 27).

To examine the spatiotemporal dynamics of apoptosis during tumorigenesis of the larval brain, we imaged *dpn^{OE}* and wild-type larval brains at different time points throughout larval development. We examined apoptosis rate of both the wild-type and the tumor brain at different developmental stages from 24 to 96 h ALH (Fig. 6*A*). At 24 h ALH, the apoptosis rate of the tumor brain was similar to that of wild-type. Surprisingly, at 36 h ALH, apoptosis rate of the *dpn^{OE}* brain was three times higher than that of the wild type (Figs. 5*F* and 6*A*). At 48 h ALH, the apoptosis rate of the tumor brain was significantly lower than that of wild-type (Figs. 5*G* and 6*A*). The apoptosis rate of the tumor brain remained low at later time points, during which the tumor brain displayed excessive growth (Fig. 6*B* and Figs. S4 and S5). Examination of more time points after larval hatching revealed intermediate stages of the apoptotic trend (Fig. S5). For example, at 30 h ALH the apoptosis rate of the tumor brains was
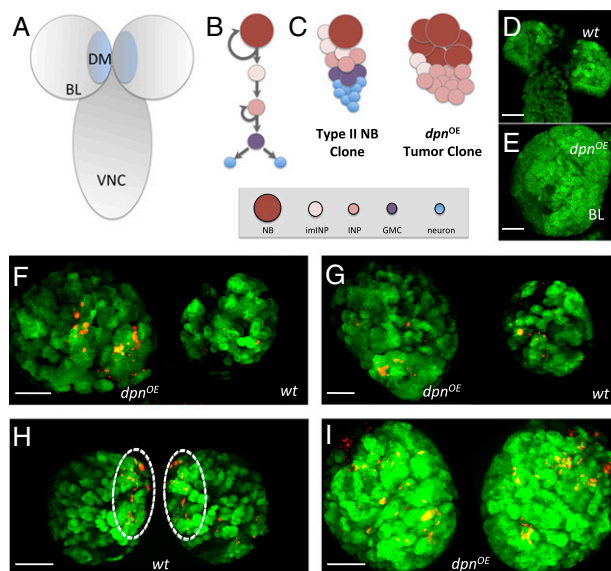

Fig. 5. iCasper reveals dynamics of apoptosis during tumorigenesis. (*A*) Schematic diagram of the *Drosophila* larval brain composed of two brain lobes (BL) and a VNC. DM: dorsal medial region. (*B*) NBs generate the neurons and glia of the adult nervous system. Type II NBs reside in the DM of each brain lobe, and undergo asymmetric divisions to self-renew and generate immature intermediate neural progenitors (imINP). The imINP will mature and asymmetrically divide to regenerate and produce a ganglion mother cell (GMC) that terminally divides into two neurons or glia. (*C*) Defects in the genes that regulate the balance between self-renewal and differentiation can lead to tumor formation. Overexpressing the self-renewal factor Dpn under the control of the inscuteable GAL-4 in NB, INPs, and GMCs leads to tumor formation. (*D*) Confocal image of a wild-type *Drosophila* larva at 72 h ALH, which reveals two brain lobes and the VNC. (Scale bar, 50 μm.) (*E*) Two-photon image of a *dpn^{OE}* tumor brain showing one brain lobe. (Scale bar, 50 μm.) (*F*) Confocal image of larval brain lobes from the tumor (*Left*) and the wild-type (*Right*) *Drosophila* at 36 h ALH. The apoptotic cells (in red) are marked by the infrared fluorescence of iCasper. (Scale bar, 30 μm.) (*G*) Confocal image of larval brain lobes from the tumor (*Left*) and the wild-type (*Right*) *Drosophila* at 48 h ALH. The apoptotic cells (in red) are marked by the infrared fluorescence of iCasper. (Scale bar, 30 μm.) (*H*) Distribution of apoptotic cells (outlined by dashed circles) in the two brain lobes of the wild type *Drosophila* at 72 h ALH. (Scale bar, 50 μm.) (*I*) Distribution of apoptotic cells in the two tumor brain lobes at 72 h ALH. (Scale bar, 50 μm.)

To et al.

between that at 24- and 36-h ALH tumor brains (Fig. S5). This finding highlights the ability of iCasper to portray the temporal dynamics of apoptosis.

Although determining the molecular mechanisms that underlie the dynamics of apoptosis would require further investigation beyond the scope of this work, it is intriguing to consider a few possible scenarios. The higher apoptosis rate in the tumor brain at 36 h ALH could result from cell overproliferation-induced apoptosis via the intrinsic tumor-suppressive network that couples cell proliferation to apoptosis and maintains tissue homeostasis (28). Interestingly, from 24 to 36 h ALH, the cell growth rate of the tumor brain was much higher than that of wild-type (Fig. 6B). On the other hand, we cannot exclude the possibility that the higher apoptosis rate could be a result of increased cell competition in the tumor brain (29). The lower apoptosis rate in the tumor brain at 48–96 h ALH might suggest that the tumor cells have evaded apoptosis. Alternatively, the lower apoptosis rate could suggest that "vulnerable" cells may have died off because of cell competition (29).

We also examined spatial distribution of apoptotic cells in the wild-type and the tumor brains. Interestingly, whereas apoptosis in the wild-type (72 h ALH) was mainly localized to the dorsal-medial region of the brain lobes (Fig. 5H and Figs. S6A and S7), the apoptotic cells in the tumor brains (72 h ALH) appeared more randomly distributed (Fig. 5I and Fig. S6B), suggesting that

the excessive growth of tumor cells may compromise structural organization of the brain (Fig. S4). Because the type II NBs reside in the dorsal-medial region of the brain (Fig. 5A), the apoptotic cells in the wild-type brain may represent members of the type II NB lineage.

We have demonstrated that iCasper reveals apoptotic dynamics during tumorigenesis. iCasper represents a useful tool for future studies examining molecular mechanisms of cancer, as well as lineage tracing of specific types of cells during normal and tumor development when combined with the large number of recently developed GAL4 lines (30–32).

Advantage of iCasper Compared with Other Caspase Reporters. Previous genetically encoded caspase reporters are not fluorogenic, which limits their applications. For example, the FRET-based reporters suffer from weak signals (within several tens percentage change of fluorescence) and require tedious image processing to obtain the ratiometric signal (33). A fluorophore translocation-based reporter was also developed, in which the fluorophore is anchored to plasma membrane and upon caspase cleavage it moves into nucleus, which limits its detection to early phase of apoptosis when there is little cell shape change (34). It is very challenging to use these nonfluorogenic reporters in detecting spatiotemporal dynamics of apoptosis in many biological processes in vivo (e.g., embryo development) because of cell heterogeneity, rapid cell shape change, and tissue movement (e.g., during morphogenesis), as well as cell and tissue autofluorescence. It is thus not surprising that the current commonly used method in detecting apoptosis in *Drosophila* and in cultured cells is based on Acridine orange staining, TUNEL, and antibody staining against cleaved caspase (35).

On the other hand, iCasper is fluorogenic, permitting straightforward detection of caspase activity, which requires no image processing. iCasper directly reports caspase activity and visualizes all phases of apoptosis from the very beginning, when the apoptotic cells start to shrink and round up to the very late stage when the apoptotic cells are disintegrated into small apoptotic cell bodies and even after they are phagocytosed by other cells. Thus, iCasper is a robust fluorogenic caspase reporter that visualizes spatiotemporal dynamics of apoptosis in vivo.

Significance of iCasper. We have demonstrated that iCasper can be used to visualize spatiotemporal dynamics of executioner-caspase activity in vivo. iCasper is a useful tool for examining the role of apoptosis in animal development and disease. It may provide insight into apoptotic signaling pathways that have proven elusive: for example, the nature and identity of developmental cues that regulate apoptosis in coordination with morphogenesis (19, 36, 37). iCasper can also be used to examine spatiotemporal dynamics of apoptosis in a number of diseases including cancer. Moreover, iCasper may be used to study apoptosis in cell-type–specific lineage tracing during normal and disease development when combined with the large number of recently developed GAL4 lines (30–32). iCasper will also be useful to dissect signaling networks that lead to apoptosis by high-throughput screening using cultured cells or small animals.

Significance of the iProtease Technology. The iProtease scaffold may be used as a core module to design reporters of all of the proteases with specific activity: for example, by direct incorporation of specific cleavage sequence into iProtease. The iProtease technology will find important applications including monitoring protease activity in a biological process in vivo, dissecting signaling pathways that regulate protease activity, and high-throughput screening of protease inhibitors for drug development and biological study.

Successful development of the iProtease technology based on the unique protein–chromophore interactions suggests that
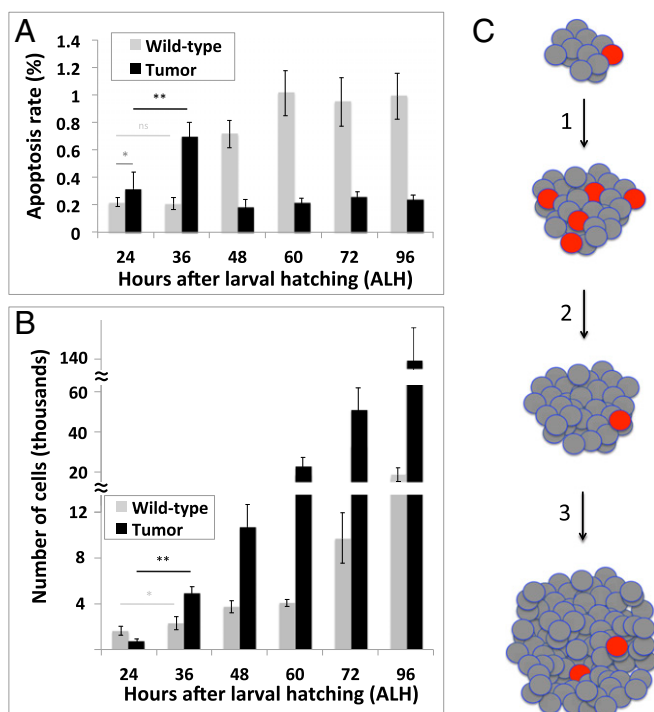

Fig. 6. Quantitative analysis of apoptosis during tumorigenesis. (*A*) Apoptosis rate in the larval brain of *Drosophila* at different stages after hatching. ns, P = not significant; $*P < 0.05$; $**P < 0.01$. (*B*) Growth of the larval brain based on the number of cells marked by GFP fluorescence at different stages after hatching. $*P < 0.05$, $**P < 0.01$. (*C*) A schematic diagram showing the dynamics of apoptosis during tumorigenesis based on the imaging data. Stage 1: At the initial stage of tumorigenesis, apoptosis rate increases significantly. One potential mechanism: cell overproliferation triggers apoptosis through an intrinsic tumor-suppressive network. Stage 2: Subsequently, apoptosis is suppressed, possibly representing tumor cell evasion of apoptosis. Stage 3: With low levels of apoptosis, the tumor grows rapidly. See alternative explanations of the dynamics of apoptosis in the text. The apoptosis rate is defined as number of infrared fluorescent cells divided by the number of green fluorescent cells in the entire brain lobe.

To et al.

www.manaraa.com

BphP-derived IFPs may provide a new and promising scaffold in designing fluorogenic reporters of, for example, kinase activity and membrane potential. Rational design of these reporters is possible by exploring the unique interactions between individual pyrrole rings of the chromophore and the surrounding residues. Furthermore, thousands of BphPs available in the protein-sequence database increase our choice of promising scaffolds. Such genetically encoded fluorogenic reporters will be ideal in visualizing spatiotemporal dynamics of cell signaling in vivo.

Materials and Methods

DNA Constructs. All of the constructs in this study are listed in Table S1.

Protein Purification. iTEV was expressed with C-terminal polyhistidine-tag on a pBAD expression vector (Invitrogen). Proteins were purified with the Ni-NTA purification system (Qiagen). Protein concentration was measured by the BCA method (Pierce). For BV production in *E. coli*, a human heme oxygenase-1 (*HO1*) gene codon optimized for *E. coli* was coexpressed on the same vector. The TEV protease was coexpressed on the same vector to generate the cleaved form of iTEV in *E. coli*. All constructs used for protein expression in *E. coli* are listed in Table S1. The protein solutions were assayed by LDS-PAGE using NuPAGE Novex 4–12% (wt/wt) Bis-Tris protein gels (Life Technologies). For zinc-induced fluorescence assay, the LDS-PAGE gel was stained with 20 mM zinc acetate at room temperature for 30 min in the dark. The zinc-induced fluorescence of the BV-bound iTEV was observed under UV light in an AlphaImager 3300 Imaging System (Alpha Innotech). All spectroscopic measurements of protein solutions were performed in PBS buffer at pH 7.4. The absorbance and fluorescence emission spectra were obtained using the Tecan Infinite M1000 micro-plate reader.

Mammalian Cell Cultures. The HEK293T/17 (ATCC CRL-11268) and LN-229 (ATCC CRL-2611) were obtained from ATCC.

Imaging Setting. Imaging was conducted using a spinning-disk confocal microscopy.

Imaging. For time-lapse live imaging of *Drosophila* embryos, the embryos were dechorionated using 1:1 diluted bleach. After washing, the embryos in running water followed by several washes in 0.1% PTx (1× PBS and 0.1% Tx-100), multiple embryos of the selected genotype were glued to a 35-mm glass-bottom dish. The glue was made by adding heptane to a small piece of Scotch tape and shaking at least overnight at room temperature. The time-lapse imaging of embryos was carried out in an incubation chamber maintained at 25 °C (see *Confocal Microscopy* in SI Materials and Methods for details). For imaging at 20× magnification, multiple embryos on the same dish were imaged over 24 h with image acquisition every 10 min. Typically, for each embryo a z-stack of 80–120 μm at an interval of 10 μm was acquired for the GFP and IFP channels. With such imaging protocol, the majority of embryos showed normal developmental progress and eventually hatched into larvae. For snapshots at 40× magnification, a z-stack at a finer interval of 2 μm was acquired over a depth of ~150 μm. On the other hand, only one to three z-planes were acquired for time-lapse imaging at 40× magnification, because prolonged light exposure at this magnification appeared to be toxic to the embryos. The light intensity from laser line was measured at 6.3 mW for 488 nm (GFP) and 13.4 mW for the 640 nm (IFP).

Image Processing. Images were processed using the ImageJ software (NIH) or the NIS-Elements Ar Microscope Imaging Software (Nikon).

1. López-Otín C, Bond JS (2008) Proteases: Multifunctional enzymes in life and disease. *J Biol Chem* 283(45):30433–30437.
2. Mason SD, Joyce JA (2011) Proteolytic networks in cancer. *Trends Cell Biol* 21(4):228–237.
3. Yu D, et al. (2014) An improved monomeric infrared fluorescent protein for neuronal and tumour brain imaging. *Nat Commun* 5:3626.
4. Shu X, et al. (2009) Mammalian expression of infrared fluorescent proteins engineered from a bacterial phytochrome. *Science* 324(5928):804–807.
5. Giraud E, Verméglio A (2008) Bacteriophytochromes in anoxygenic photosynthetic bacteria. *Photosynth Res* 97(2):141–153.
6. Wagner JR, Brunzelle JS, Forest KT, Vierstra RD (2005) A light-sensing knot revealed by the structure of the chromophore-binding domain of phytochrome. *Nature* 438(7066):325–331.
7. Cabantous S, Terwilliger TC, Waldo GS (2005) Protein tagging and detection with engineered self-assembling fragments of green fluorescent protein. *Nat Biotechnol* 23(1):102–107.
8. Bhoo SH, Davis SJ, Walker J, Karniol B, Vierstra RD (2001) Bacteriophytochromes are photochromic histidine kinases using a biliverdin chromophore. *Nature* 414(6865):776–779.
9. Berkelman TR, Lagarias JC (1986) Visualization of bilin-linked peptides and proteins in polyacrylamide gels. *Anal Biochem* 156(1):194–201.
10. Chae HJ, et al. (2000) Molecular mechanism of staurosporine-induced apoptosis in osteoblasts. *Pharmacol Res* 42(4):373–381.
11. Rehm M, et al. (2002) Single-cell fluorescence resonance energy transfer analysis demonstrates that caspase activation during apoptosis is a rapid process. Role of caspase-3. *J Biol Chem* 277(27):24506–24514.
12. Page DT, Olofsson B (2008) Multiple roles for apoptosis facilitating condensation of the *Drosophila* ventral nerve cord. *Genesis* 46(2):61–68.
13. Rogulja-Ortmann A, Lüer K, Seibert J, Rickert C, Technau GM (2007) Programmed cell death in the embryonic central nervous system of *Drosophila* melanogaster. *Development* 134(1):105–116.
14. Hay BA, Wolff T, Rubin GM (1994) Expression of baculovirus P35 prevents cell death in *Drosophila*. *Development* 120(8):2121–2129.
15. Suzanne M, Steller H (2013) Shaping organisms with apoptosis. *Cell Death Differ* 20(5):669–675.
16. Ndozangue-Touriguine O, Hamelin J, Bréard J (2008) Cytoskeleton and apoptosis. *Biochem Pharmacol* 76(1):11–18.
17. Charras GT, Yarrow JC, Horton MA, Mahadevan L, Mitchison TJ (2005) Non-equilibration of hydrostatic pressure in blebbing cells. *Nature* 435(7040):365–369.
18. Conradt B (2009) Genetic control of programmed cell death during animal development. *Annu Rev Genet* 43:493–523.
19. Fuchs Y, Steller H (2011) Programmed cell death in animal development and disease. *Cell* 147(4):742–758.
20. Nassif C, Daniel A, Lengyel JA, Hartenstein V (1998) The role of morphogenetic cell death during *Drosophila* embryonic head development. *Dev Biol* 197(2):170–186.
21. Hanahan D, Weinberg RA (2011) Hallmarks of cancer: the next generation. *Cell* 144(5):646–674.
22. Zhu S, et al. (2012) The bHLH repressor Deadpan regulates the self-renewal and specification of *Drosophila* larval neural stem cells independently of Notch. *PLoS ONE* 7(10):e46724.
23. Zacharioudaki E, Magadi SS, Delidakis C (2012) bHLH-O proteins are crucial for *Drosophila* neuroblast self-renewal and mediate Notch-induced overproliferation. *Development* 139(7):1258–1269.
24. San-Juán BP, Baonza A (2011) The bHLH factor deadpan is a direct target of Notch signaling and regulates neuroblast self-renewal in *Drosophila*. *Dev Biol* 352(1):70–82.
25. Homem CCF, Knoblich JA (2012) *Drosophila* neuroblasts: A model for stem cell biology. *Development* 139(23):4297–4310.
26. Doe CQ (2008) Neural stem cells: Balancing self-renewal with differentiation. *Development* 135(9):1575–1587.
27. Wallace K, Liu TH, Vaessin H (2000) The pan-neural bHLH proteins DEADPAN and ASENSE regulate mitotic activity and cdk inhibitor dacapo expression in the *Drosophila* larval optic lobes. *Genesis* 26(1):77–85.
28. Lowe SW, Cepero E, Evan G (2004) Intrinsic tumour suppression. *Nature* 432(7015):307–315.
29. Amoyel M, Bach EA (2014) Cell competition: How to eliminate your neighbours. *Development* 141(5):988–1000.
30. Manning L, et al. (2012) A resource for manipulating gene expression and analyzing cis-regulatory modules in the *Drosophila* CNS. *Cell Reports* 2(4):1002–1013.
31. Jenett A, et al. (2012) A GAL4-driver line resource for *Drosophila* neurobiology. *Cell Reports* 2(4):991–1001.
32. Jory A, et al. (2012) A survey of 6,300 genomic fragments for cis-regulatory activity in the imaginal discs of *Drosophila* melanogaster. *Cell Reports* 2(4):1014–1024.
33. Takemoto K, et al. (2007) Local initiation of caspase activation in *Drosophila* salivary gland programmed cell death in vivo. *Proc Natl Acad Sci USA* 104(33):13367–13372.
34. Bardet P-L, et al. (2008) A fluorescent reporter of caspase activity for live imaging. *Proc Natl Acad Sci USA* 105(37):13901–13905.
35. Sarkissian T, Timmons A, Arya R, Abdelwahid E, White K (2014) Detecting apoptosis in *Drosophila* tissues and cells. *Methods* 68(1):89–96.
36. Mollereau B (2009) Cell death: What can we learn from flies? Editorial for the special review issue on *Drosophila* apoptosis. *Apoptosis* 14(8):929–934.
37. Lin N, Zhang C, Pang J, Zhou L (2009) By design or by chance: Cell death during *Drosophila* embryogenesis. *Apoptosis* 14(8):935–942.

BIOCHEMISTRY

www.manaraa.com